Design of Battery Electrodes with Dual-Scale Porosity to Minimize Tortuosity and Maximize Performance

Chang-Jun Bae, Can K. Erdonmez, John W. Halloran, and Yet-Ming Chiang*

Advances in materials and electrode architecture have facilitated remarkable improvements in the power performance of rechargeable batteries over the past decade, as represented by laboratory demonstrations of fast discharge[1–3] and commercial realizations such as packaged Li-ion cells with >20 kW/kg at ~65 Wh/kg.[4] However, even the most advanced of today's batteries continue to have poor materials utilization, with only ~50% of cell volume devoted to active materials in cells designed for high-energy density.[5] Thus, emphasis has now shifted towards maximizing energy density while retaining sufficient rate capability to power critical applications such as portable devices and electric vehicles. In batteries using porous electrodes, cell-level energy density increases with electrode thickness and density, until limitations on accessible capacity are imposed by inadequate ion transport through a diminishing volume of tortuous, electrolyte-filled porosity.[6,7] For electrodes in which electronic conductivity and charge-transfer are not rate-limiting, ion transport in the percolating electrolyte network becomes limiting as current density increases beyond a critical value.[6,8] Since tortuosity τ, increases non-linearly with density (e.g., following the Bruggeman relationship $\tau \propto \varepsilon^{-1/2}$, where ε is pore fraction), attempts to increase cell energy density by densifying the electrodes rapidly reach diminishing returns. (Throughout, we define $\tau = \varepsilon(\sigma_0/\sigma)$, with ε the volume fraction porosity, σ a measured transport coefficient, and σ_0 the value of the transport coefficient for the pore-filling medium). Efforts to increase cell-level energy density by increasing electrode thickness (i.e., reducing inactive materials such as separators and current collectors) likewise incur electrolyte-transport limitations. Measured electrode tortuosities vary widely with electrode porosity and preparation, but commonly range between 2.5–30,[8–10] implying significant room

for improvement. Electrode topology control such as spatially ordered macroporous structures[11,12] and multimodal/hierarchical pore size distributions[13–15] have been demonstrated to provide higher power, and now there is increasing attention to the impact on energy density as well.[3,16,17] There persists a need for scalable electrode designs and fabrication methods that maximize energy density while meeting C-rates relevant to broad classes of applications.

Here, we identify theoretically and experimentally an ordered, "dual-scale" porosity distribution that maximizes power at a given pore fraction and thickness by minimizing electrode tortuosity. We test the general predictions of the model, and demonstrate one scalable path to such designs, by employing iterative co-extrusion and sintering to fabricate electrodes with porosity partitioned between a porous matrix and low-tortuosity channels of periodicity down to ~15 μm. Compared with optimized conventional Li-ion electrodes,[7] approximately threefold higher capacity per unit area (mAh/cm²) is achieved at relevant 1C-2C discharge rates. The fundamental question addressed here is whether periodic pore channels of unit tortuosity, embedded in a porous matrix (**Figure 1**A), can improve ion transport under conditions of *fixed total porosity* (i.e., fixed electrode energy density, with aligned porosity being introduced at the expense of reduced matrix porosity.) The general problem of how to disperse a finite volume of high-conductance elements throughout a medium is encountered elsewhere in both nature and engineering, with various geometric strategies being available for problems in heat, mass or charge transport.[18–20] There are branching/"vascular", graded or aligned structures that are appealing to consider, but challenging to fabricate. We therefore choose to model and test a porosity distribution that is amenable to economical powder based processing, and lies between the idealized limit of a dense electrode with appropriately spaced straight channels (of $\tau = 1$), and the unmodified limit of homogeneous random porosity, e.g., as determined by particle packing. We estimate *effective electrode tortuosity* for all possible arrangements of the channel array. Experiments are conducted using an electrode fabrication approach that allows the pore channel spacing and diameter to be scaled over three orders of magnitude. Our best electrodes allow discharge rates up to 2C with near-theoretical capacity utilization at areal capacities (mAh/cm²) that are three times those of optimized Li-ion battery electrodes.

The structure under consideration (Figure 1), is modeled as a periodic array of cylindrical channels forming "unit cells" with a porous matrix surrounding each channel. When electrode thickness, T, and overall electrode porosity, P, are fixed, so are the charge capacity per unit area of current collector (areal capacity, mAh/cm²) and the energy density of the electrode (Wh/L). The remaining parameters defining a design,

Dr. C.-J. Bae,[+,++] Prof. Y.-M. Chiang
Materials Science and Engineering
Massachusetts Institute of Technology
Cambridge, MA 02139, USA
E-mail: ychiang@mit.edu
Dr. C. K. Erdonmez[+]
Energy Storage Group
Brookhaven National Laboratory
Upton, NY 11973, USA
Prof. J. W. Halloran
Materials Science and Engineering
University of Michigan
Ann Arbor, MI 48109, USA
[+]C.J.B. and C.K.E. contributed equally to this work.
[++]Present address: Hardware System Laboratory, Palo Alto Research Center (PARC), 3333 Coyote Hill Road, Palo Alto, CA 94304, USA
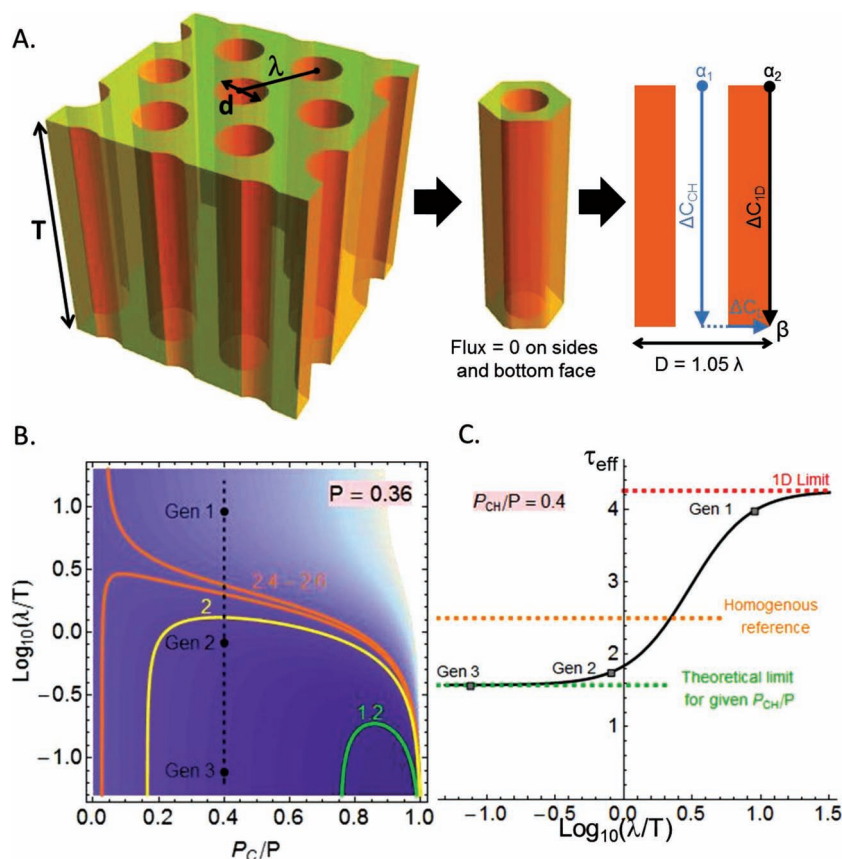
Figure 1. Periodic channel array threading across a porous matrix of sintered active particles. A) Decomposition into hexagonal unit cells, further approximated as cylindrical cells of same volume. B) Contour plot of effective electrode tortuosity, based on electrolyte concentration drop across the electrode during discharge under a steady-state assumption. The case for 36% overall porosity is shown. The darker background colors correspond to lower tortuosities. C) Improved power performance is guaranteed for $\lambda \ll T$ (experimentally corresponding to our sample Gen 3), likely for $\lambda \sim T$ (Gen 2). For $\lambda > T$ (Gen 1), "1D" transport inside the porous matrix, parallel to the channels, dominates, yielding higher effective tortuosity than in a homogenous monolith of the same overall porosity.

are λ, the channel spacing, and P_C, the pore fraction of the channels. P_C is bounded by zero for a homogenous electrode and P for a fully dense matrix with all porosity located within channels. The channel diameter and matrix porosity, ε, are also fixed upon selecting P, λ and P_C. The channel is assigned unit tortuosity, while tortuosity in the porous matrix follows a modified Bruggeman relationship, $\tau = \gamma \varepsilon^{-1/2}$, in which the coefficient γ is assumed equal to 1.5, corresponding to sintered ceramics having porosity $\varepsilon = 0.15$–0.5.[21] The porous electrode model of Doyle and Newman[6] is modified to obtain the *steady state concentration drop across the electrode during discharge*, ΔC. For the electrode in Figure 1A, bounded by a separator above and a current collector below, there exist two limiting paths for ion transport from location α across the electrode to location β. One path (blue arrows in Figure 1A) is along the channel and then laterally across the matrix; the second path (black arrow) is through the porous matrix alone, parallel to the channels. For either path, an effective tortuosity is found by calculating ΔC and comparing to the value for an electrode of unit tortuosity. When the limiting paths are comparably effective, we estimate

the net tortuosity by interpolating between the two limits using the addition rule for parallel resistors. Additional details are given in Supporting Information.

Results from the analysis are shown in Figures 1B and C for total porosity P = 0.36, corresponding to experiments discussed later. The channel spacing relative to electrode thickness, (λ/T), and the channel pore fraction, (P_C/P), emerge as logical independent variables. Figure 1B shows *iso-tortuosity contours* for τ_{eff} as a function of (P_C/P) and $\log_{10}(\lambda/T)$. Orange contours mark a small (±4%) range around $\tau_{eff} = 2.5$, the value for a homogenous electrode with P = 0.36 (modified Bruggeman relation). Above these contours, effective tortuosity is *higher* than in the homogenous case. For example, to the upper right in the figure, nearly all available porosity appears in large but widely-spaced channels, with the consequence that transport in the dense, high-tortuosity matrix becomes rate-limiting. The yellow contour denotes τ_{eff} lower by 20% than the homogenous value, obtained, e.g. with a small volume of channels with $\lambda/T = 1$. Towards the lower right in Figure 1B, one approaches an idealized structure of unit tortuosity, resulting when all porosity appears as straight channels with vanishingly small spacings. Such structures are effective but likely impractical to fabricate at low cost and in large scale. However, Figure 1B also shows that tortuosities close to unity are achievable with λ/T in the range 0.1–1, constituting reasonable objectives for scaleable processing. The green contour marks designs within 20% of the achievable minimum; as an example, with 80% of porosity appearing inside channels, i.e. (P_C/P) = 0.8, $\tau_{eff} = 1.2$ only requires $\lambda \sim T/6$.

To illustrate further, a section of the τ_{eff} surface in Figure 1B, along the vertical dashed line, is plotted in Figure 1C. This section represents the present experiments, in which (P_C/P) ~ 0.4. Limiting behaviors for large and small channel spacings are indicated, as well as the value for the homogenous case. The upper limit corresponds to the instance where channels are too far apart to be effective and diffusion occurs mainly through the matrix. Here, the tortuosity is actually *higher* than the homogenous value because 40% of the available porosity is devoted to channels. For the lower limit, transport through the channels predominates; tortuosity is reduced but does not reach unity since 60% of porosity remains in the matrix. The asymptotic approach to the limiting tortuosity toward the left in Figure 1C confirms that reducing λ/T below ~0.1 provides diminishing returns. Thus, our analysis identifies the largest relative spacings, λ/T, that provide essentially all of the benefits of straight pore channels.

A scalable powder-based fabrication method that provides λ/T of this order was then developed, which yielded samples

having values of (λ/T) labeled "Gen 1, Gen 2, Gen3" in Figure 1C. This fabrication approach combines two recent developments: sintered porous monoliths of active materials as high energy density battery electrodes,[22] and co-extrusion down to feature sizes ≤ 5 μm.[23] The sintering approach allows preparation of electrodes fully free of binders and additives and therefore maximizes energy density. We selected $LiCoO_2$ as a model active material that is free of electronic conductivity limitations[22] due to a semiconductor-metal transition that occurs upon slight delithiation.[24] Furthermore, in our experience, sintered porous monoliths of this material are capable of stable electrochemical cycling, with little to no capacity fade, for at least 250 cycles. Extrusion has a long history in large-scale production of ceramic and glass structures such as honeycombs, tubes, filters and tissue scaffolds, typically with cross-section feature sizes exceeding 50 μm. To obtain aligned channels with smaller periodicity, we iteratively extruded linear elements, **Figure 2**.[25] Each co-extrusion pass reduces feature sizes in the electrode plane by a constant factor, while overall electrode density remains constant. Compared to micro- or nano-fabrication processes such as vapor deposition, lithographic etching or laser-machining, we achieve much higher fabrication rates.

The fabrication process starts with a feedrod prepared from a mixture of $LiCoO_2$ powder and polymeric binder; an axial core of a similar carbon-binder mixture is then inserted into the feedrod. Both the carbon and the polymer binders are later removed by pyrolysis during sintering. The feedrod is extruded through a die with a reduction ratio of 11. The extruded fiber is then sectioned, re-assembled into a structure with diameter equal to the initial feedrod, and extruded again. Optical images of the starting material and three subsequent generations are shown in Figure 2; design parameters for these generations is summarized in Table S1 of the Supporting Information (SI). Gen 0 is the initial feedrod (diameter ~22 mm and channel diameter ~7.5 mm. After three extrusion iterations followed by pyrolysis and sintering, we obtain the Gen 3 structure, with channels of ~6 μm diameter and center spacings of λ~17 μm.

Figure 3 shows SEM images from the Gen 3 structure (Figure S2 of the SI contains a comparison with Gen 2). The channel diameters and spacings are as expected from three 11-fold reductions of the initial feedrod (Figures 3A & 3B). Images of the top surface,
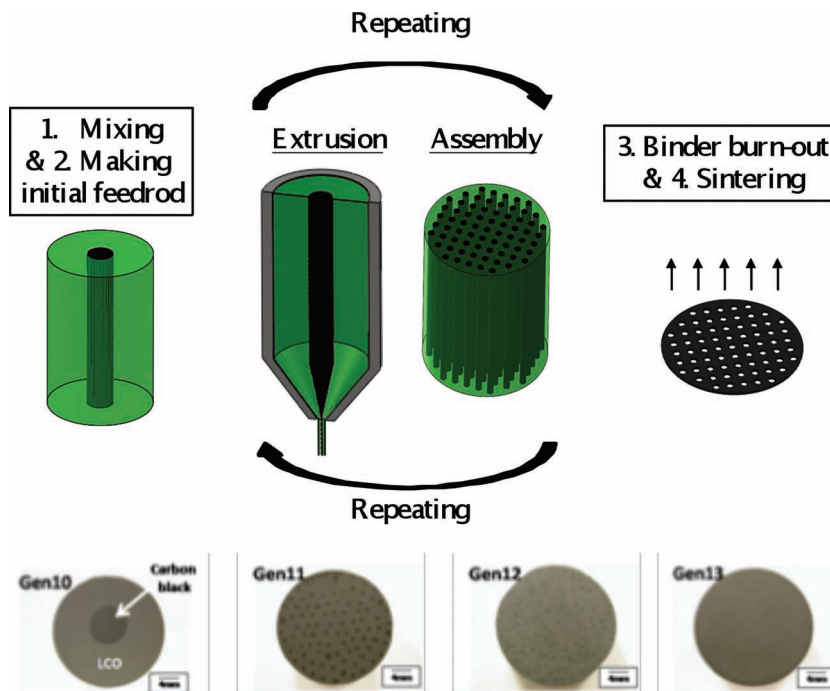

Figure 2. Outline of the electrode fabrication process. Co-extrusion produces macro-pore channels, with controlled channel spacings. Lower row shows optical images of the green body before binder burn-out and sintering for different sample generations. Gen 0, Gen 1, Gen 2, and Gen 3 correspond, respectively, to the initial feed rod and the assembled structures after the 1st, 2nd, and 3rd extrusion passes. The darker dots (visible to the eye in Gens 0–2) are composed of carbon black and polymeric binder and leave aligned macro-pore channels after burn-out.
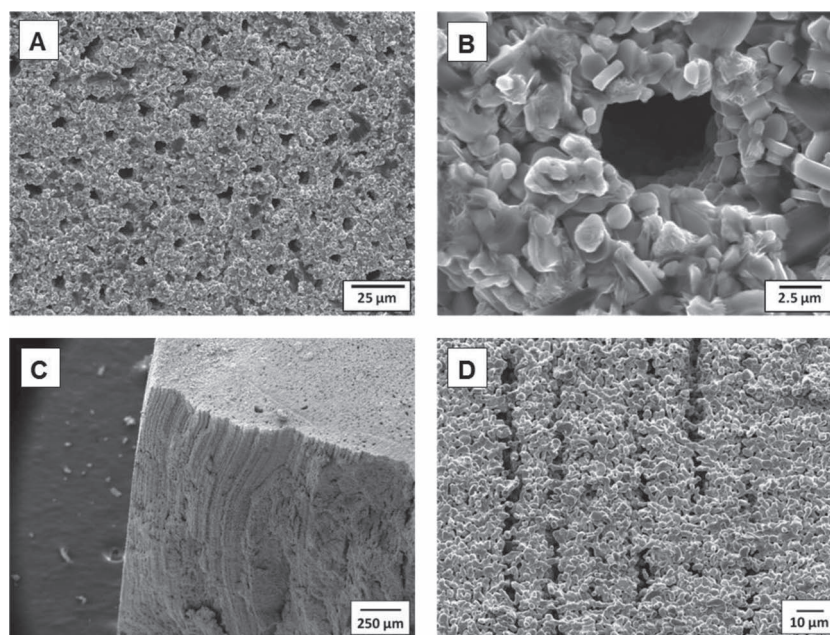

Figure 3. Gen 3 sample microstructure, generated by three co-extrusion iterations followed by binder burn-out and sintering. A) Low-, and B) high-magnification SEM images showing polished top surfaces. C) Low-, and D) high-magnification SEM images of sample in cross-section. This electrode has aligned channels ~6 micrometers in diameter, with an average channel spacing of 17 micrometers.

as well as fracture surfaces (Figure 3C) and cross-sections (Figure 3D), show that channels remain open over lengths of tens to hundreds of micrometers. Deformation that results when fibers are pressed prior to re-extrusion produces somewhat curved channels near the sample edges (Figure 3C). The matrix pore size remains constant through successive generations, being dictated mainly by the sintering temperature. Gen 2 and Gen 3 samples sintered at 1000 °C both possess an average matrix pore diameter of ~1 μm whereas a Gen 3 electrode sintered at 1050 °C showed increased matrix density and smaller pores. While the high-aspect-ratio channels should eventually break up into isolated segments due to Rayleigh instability,[26] in our experience, the porous matrix densifies noticeably first, allowing us to sinter particles in the matrix to high densities while preserving continuous channels.

Sintered electrodes of 220 μm thickness were prepared from each of the three generations of co-extruded structures, and from homogenous material of matching overall porosity as controls. These were electrochemically cycled against a Li⁰ reference, with charging at C/15 rate and discharge at various rates. **Figure 4**A shows discharge capacity versus discharge rate for an electrode sintered at 1000 °C (62% overall density, ~75% matrix density), and Figure 4B shows voltage-capacity

Figure 4. A) Specific capacity vs discharge rate and, B) voltage vs discharge capacity for electrodes with overall density of 62%, compared to a homogeneously porous reference sample. Gen 2 and Gen 3 samples show improved capacity retention as average channel spacing is decreased, to 180 μm and 17 μm, respectively (see also Table S1 of the SI). C) Areal capacity (mAh/cm²) vs.C-rate for present electrodes (Gen 3) compared to optimized Li-ion electrodes[7] using Li(Ni,Mn,Co)O₂ and LiFePO₄ active materials, showing a three-fold improvement in areal capacity at practical current rates of 1C–2C for the former.

discharge curves at selected C-rates. Corresponding data from otherwise identical samples sintered at 1050 °C (70% overall density, ~81% matrix density) appear in Figure S3 of the SI. For either value of overall density, each generation shows improved capacity retention with increasing C-rate over the preceding generation. At low discharge rates (C/15), the discharge capacity and voltage-capacity curves of all 62% dense samples are essentially identical (Figure 4B), but with increasing C-rate, each generation shows improved capacity retention over the preceding generation (similar results are seen for the 70% dense samples (Figure S3 of the SI). At 2C rate, it is clear that the highest generation number exhibits the highest discharge capacity and smallest polarization. Given that each generation is identical to the previous one except for channel spacing λ, the results unambiguously show that reducing lateral diffusion lengths between channels enhances overall ion-transport. The best-performing structure, Gen 3, delivers the same capacity as the homogenous controls at 2 to 3 times the discharge rate, consistent with the predicted reduction of net tortuosity (Figure 1C).

As was also predicted, structures with coarse channel spacing such as Gen 1 underperform compared to the homogenous controls (marked "Ref" in figures) in terms of rate capability (Figures 4A and Figure S3A of the SI) and polarization (Figures 4B and Figure S3B of the SI). In other words, introducing channels at lower resolutions *degrades* performance at the same total porosity (and energy density). The role of matrix density is also interesting. Our best-performing samples,
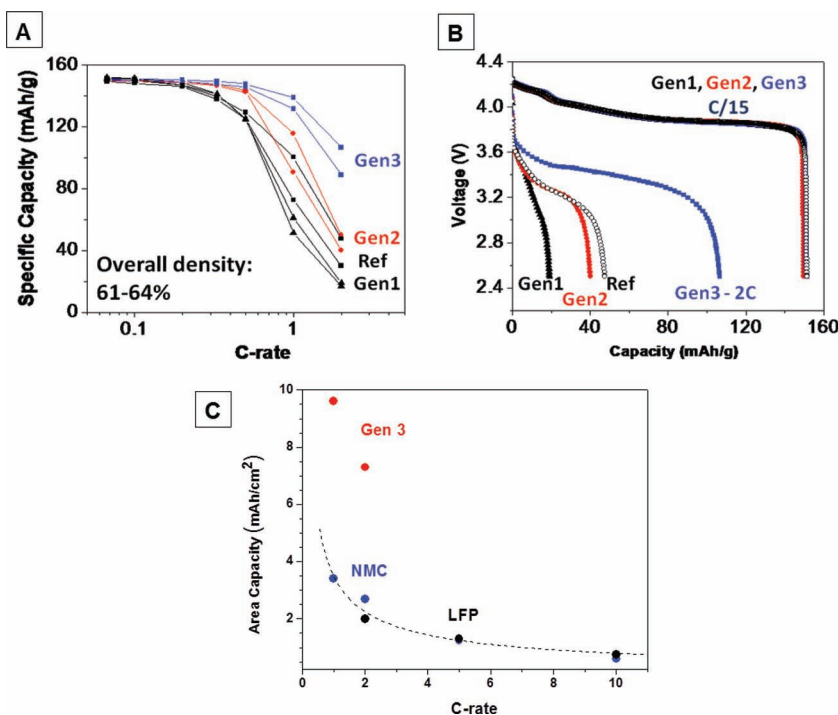
sintered at 1000 °C, have a high matrix density of 75%. Upon further densifying the matrix to 81%, there is a significant fall-off in power which may be due to formation of closed porosity.

We now compare our results to recent systematic studies of the maximum working C-rate for conventional cathodes as a function of their areal capacity (Figure 4C). Zheng et al.[7] found very similar power law relationships between areal capacity and maximum C-rate for conventional cathodes prepared with NMC and LFP active materials. The essentially common scaling of capacity versus C-rate with variable electrode thickness (up to ~100 μm) with all other experimental parameters held constant, was attributed to ion transport limitations in the electrolyte, as in our case. Comparing at 2C rate, a practical upper limit for most portable device and PHEV/EV applications, Figure 4C shows that our sintered, dual-scale electrodes provide almost 3 times the areal capacity. In practical terms, this could allow proportionately fewer separator layers, current collectors layers, tabs, and packaging for the same energy, thereby improving cell-level energy density and reducing costs associated with the electrochemically inactive components.

In summary, we have demonstrated a general approach to improving electrode kinetics in which available porosity is distributed at multiple length scales to reduce the effective tortuosity of the pore network. Regimes under which net tortuosity increases, as well as decreases, relative to a homogenous electrode are identified for low-tortuosity channels threading across a porous electrode. Experimental validation has been

obtained using sintered LiCoO$_2$ cathodes that closely match the model architecture. The process of repeated coextrusion/assembly followed by sintering developed here allows scaling of channel diameters and spacings (down to ~5 and ~15 μm respectively) as well as of the matrix density. Our approach can be adopted generally and motivates further development of scaleable, low-cost manufacturing methods to manipulate electrode pore topology.

Experimental Section

Preparation of Porous Cathodes with Dual-Scale Porosity: Thermoplastic mixtures were prepared by blending fine powder of the active material, LiCoO$_2$, or the fugitive pore former, carbon black, with poly(ethylene-co-ethyl acrylate) (EEA 6182; Union Carbide, Danbury, CT) and poly(isobutyl methacrylate) (Acryloid B67; Rohm and Haas, Philadelphia, PA) as polymer binders, along with other additives. A typical composition, by weight for the mixture containing the active particles was 85% LiCoO2, 9% poly(ethylene-co-ethyl acrylate), 4% poly(isobutyl methacrylate), 1% poly ethylene glycol, 0.7% mineral oil and 0.3% stearic acid. The thermoplastic binders were fused at 120 °C in a heated shear mixer (PlasticCorder PL 2100 Electronic Torque Rheometer; C. W. Brabender, South Hackensack, NJ). Powder (LiCoO$_2$ or carbon black) and processing aids such as heavy mineral oil (Kaydol; Sonneborn, Petrolia, PA), polyethylene glycol (PEG 1000; Acros Organics, NJ, USA), and stearic Acid (A12244; Alfa Aesar, Ward Hill, MA) were added as necessary to the melted binders in order to reduce viscosity, improve dispersion of the powder, and obtain consistent rheological flow behavior. Once blended, the carbon black thermoplastic compound was uniaxially pressed into a 7 mm cylindrical die at 10 MPa and 145 °C. The LiCoO$_2$ thermoplastic compound was pressed into a 22 mm cylindrical die under the same pressure and temperature, a 7 mm diameter cylindrical hole machined at its center, and the carbon black rod inserted to create the initial feedrod. The completed feedrod was then extruded through a symmetric 11:1 circle reduction die at 110 °C using a piston extruder. The extrudate was sliced and assembled into a structure with diameter equal to the initial feedrod. The assembly was uniaxially pressed at 10 MPa and 145 °C to create a second feedrod and re-extruded. After the desired number of iterations, the pressed assemblies were cut to 0.5 mm thickness, and heat treated to 200–600 °C in air for binder burn-out, followed by sintering at the indicated experimental temperatures.

Electrochemical Testing: Square electrode samples (6 mm × 6 mm area) were electrochemically tested against lithium foil electrodes in Swagelok-type cells with stainless-steel current collectors. Two layers of Celgard 2500 microporous separator were used. The liquid electrolyte consisted of 1.3 M LiPF$_6$ in a blend of alkyl carbonates. Cells were cycled using a galvanostat/potentiostat/impedance analyzer (Bio-logic VMP3). CCCV charging was used, with constant (C/15) current applied until cell voltage reached a selected value (4.25 V). This voltage was held until current decayed to a chosen cutoff (C/50). A 1-h rest step followed, after which cells were galvanostatically discharged at various rates to 2.5 V.

Supporting Information

Supporting Information is available from the Wiley Online Library or from the author.

[1] S.-Y. Chung, J. T. Bloking, Y.-M. Chiang, *Nature Mater.* **2002**, *1*, 123.

[2] B. Kang, G. Ceder, *Nature.* **2009**, *458*, 190.

[3] H. Zhang, X. Yu, P. V. Braun, *Nature Nanotech.* **2011**, *6*, 277.

[4] http://www.A123Systems.com/customer-case-study-mercedes-benz-high-performance-engines (accessed November 2012).

[5] R. Moshtev, B. Johnson, *J. Power Sources* **2000**, *91*, 86.

[6] M. Doyle, J. Newman, *J. Appl. Electrochem.* **1997**, *27*, 846.

[7] H. Zheng, J. Li, X. Song, G. Liu, V. S. Battaglia, *Electrochimica Acta* **2012**, *71*, 258.

[8] P. A. Johns, M. R. Roberts, Y. Wakizaka, J. H. Sanders, J. R. Owen, *Electrochem. Comm.* **2009**, *11*, 2089.

[9] I. V. Thorat, D. E. Stephenson, N. A. Zacharias, K. Zaghib, J. N. Harb, D. R. Wheeler, *J. Power Sources* **2009**, *188*, 592.

[10] N. Mellgren, S. Brown, M. Vynnycky, G. Lindbergh, *J. Electrochem. Soc.* **2008**, *155*, A304.

[11] J. S. Sakamoto, B. Dunn, *J. Mater. Chem.* **2002**, *12*, 2859.

[12] N. S. Ergang et al., *Adv. Mater.* **2006**, *18*, 1750.

[13] Y. S. Hu et al., *Adv. Funct. Mater.* **2007**, *17*, 1873.

[14] B. Fang, M.-S. Kim, J. H. Kim, S. Lim, J.-S. Yu, *J. Mater. Chem.* **2010**, *20*, 10253.

[15] Y.-G. Guo, Y.-S. Hu, W. Sigle, J. Maier, *Adv. Mater.* **2007**, *19*, 2087.

[16] M. Gaberscek, R. Dominko, R. M. Bele, M. Remskar, J. Jamnik, *Solid State Ionics* **2006**, *177*, 3015.

[17] R. Dominko et al., *Chem Mater.* **2007**, *19*, 2960.

[18] G. B. West, J. H. Brown, B. J. Enquist, *Science* **1999**, *284*, 1677.

[19] N. Dan, A. Bejan, *J. Appl. Phys.* **1998**, *84*, 3042.

[20] V. Ramadesigan, R. N. Methekar, F. Latinwo, R. D. Braatz, V. R. Subramanian, *J. Electrochem. Soc.* **2010**, *157*, A1328.

[21] M. Bernard, G. A. Williams, *Phys. Rev. Lett.* **1991**, *67*, 2585

[22] W Lai et al., *Adv. Mater.* **2010**, *22*, E139.

[23] M. Bayindir, F. Sorin, A. F. Abouraddy, J. Viens, J. D. Joannopoulos, Y. Fink, *Nature* **2004**, *431*, 826.

[24] J. Molenda, A. Stoklosa, T. Bak, *Solid State Ionics* **1989**, *36*, 53.

[25] A. Crumm, J. W. Halloran, *J. Am. Cer. Soc.* **1998**, *81*, 1053.

[26] W. C. Carter, A. M. Glaeser, *Acta Metall.* **1987**, *35*, 237.